J. Fluid Mech. (1999), *vol.* 389, *pp.* 229–254. Printed in the United Kingdom

Wavelet analyses of velocities in laboratory isotropic turbulence

By H. MOURI[1], H. KUBOTANI[2], T. FUJITANI[1], H. NIINO[3] AND M. TAKAOKA[4]

[1] Meteorological Research Institute, Nagamine 1-1, Tsukuba 305, Japan

[2] Institute of Computer Science, Faculty of Engineering, Kanagawa University, Kanagawa, Yokohama 221, Japan

[3] Ocean Research Institute, University of Tokyo, Nakano, Tokyo 164, Japan

[4] Division of Physics and Astronomy, Graduate School of Science, Kyoto University, Kyoto 606-01, Japan

(Received 11 June 1997 and in revised form 10 December 1998)

Orthonormal wavelet transformations are used to decompose velocity signals of grid turbulence into both space and scale. The transforms exhibit small-scale enhancements of (i) the spatial fluctuation, (ii) the correlation in space between the adjacent scales, and (iii) the correlation in space between the longitudinal and transverse components. The spatial fluctuation and the scale–scale correlation at small scales are more significant in the transverse component than in the longitudinal component. These features are the same for different families of wavelets.

Turbulence contains tube-like structures of vorticity. We demonstrate that wavelet transforms of velocities are enhanced at the positions of the tubes, by using a direct numerical simulation. Thus our wavelet analyses have captured the effects of those coherent structures on velocities measured in the experiment, which would be difficult for traditional analysis techniques such as those with velocity increments.

1. Introduction

The classical theory of Kolmogorov (1941*a*) postulates that turbulence is space-filling at all scales, from the largest scales where the kinetic energy is input, to the smallest scales where the kinetic energy is converted into the thermal energy. However, in practice, the small-scale fluid motion is active only in a fraction of the volume (Batchelor & Townsend 1949). This phenomenon of ‘intermittency’ is crucial to our understanding of turbulence (see Nelkin 1994; Frisch 1995; or Sreenivasan & Antonia 1997 for a review).

Experiments on turbulence are usually made with a single probe suspended in a flow. Then the standard procedure is to compute the velocity increment $u(x+\delta)-u(x)$, where $u(x+\delta)$ and $u(x)$ are velocities at two points separated by a distance δ in the mean-flow direction. Though invaluable information on intermittency is obtained from statistics of the increments for the individual scales (Anselmet *et al.* 1984), more rigorous space–scale decompositions of the velocity data are required to proceed further. This situation calls for a new approach using ‘orthonormal wavelets’, which are self-similar functions localized both in space and scale.

There are several known families of orthonormal wavelets (Haar 1910; Meyer 1985–1986; Daubechies 1988; Mouri & Kubotani 1995). A wavelet family constitutes a complete orthonormal transformation, being analogous to the Fourier transformation based on sinusoidal functions. The transform corresponds to variations in the signal at a given scale and a given point, because a wavelet function has a zero mean. Hence there is a close resemblance of wavelet transforms of a certain scale to velocity increments over such a scale (Yamada & Ohkitani 1991; Meneveau 1991). We underline that wavelet transforms are more focused on given scales and thus preferable for studying the intermittent structures.

The space–scale decomposition has already been realized by band-pass filtering techniques (Kuo & Corrsin 1971) and redundant transformations based on 'continuous (non-orthonormal) wavelets' (Argoul *et al.* 1989; Farge 1992). However, our approach is different from theirs. Orthonormal wavelets have a unique advantage that the transforms are mutually independent and retain the same information as the original data. This advantage makes the interpretation of the results more reliable, especially in the cases of statistical studies (Yamada & Ohkitani 1991; Meneveau 1991).

Following the pioneering works of Yamada & Ohkitani (1991) and Meneveau (1991), we apply orthonormal wavelets to statistical analyses of turbulent velocity fields. Our analyses are conducted with five different families of wavelets (§ 2), in order to assess the reliability of the results with respect to the choice of wavelet. The data to be studied are of both the longitudinal and transverse velocities obtained from a laboratory measurement of a flow behind a grid (§ 3). We introduce wavelet diagnostics of intermittency, and calculate them from our data (§ 4). Turbulence is believed to contain structures of vorticity and dissipation rate. We discuss our results in connection with those structures, by using a direct numerical simulation of homogeneous three-dimensional turbulence (§ 5).

2. Orthonormal wavelet transformation

This section explains the concept of orthonormal wavelets in the framework of 'multi-resolution analyses' (Mallat 1989). We do not go into the details: readers are referred to the review by Farge (1992). We also discuss how to interpret the transforms of the velocity data.

2.1. *Wavelets*

Wavelet transformations are constructed on the basis of a 'mother wavelet' $w(x)$ and a 'scaling function' $s(x)$. They are localized both in space and scale. The mother wavelet has a zero mean and thus extracts variations of a signal. The scaling function, the integral of which from $-\infty$ to $+\infty$ is unity, is an averaging function. From the mother wavelet, the wavelet functions $w_{j,k}(x)$ are created through discrete dilation and translation:

$$w_{j,k}(x) = 2^{j/2}\, w(2^j x - k) \quad (j, k \in Z). \tag{1}$$

The indices j and k specify the scale of the wavelet and its position on the x-axis, respectively. Likewise, we have

$$s_{J,k}(x) = 2^{J/2}\, s(2^J x - k) \quad (J \in Z). \tag{2}$$

Then any square-integrable function $u(x)$ is reconstructed as

$$u(x) = \sum_{k=-\infty}^{+\infty} \bar{u}_{J,k}\, s_{J,k}(x) + \sum_{j=J}^{+\infty} \sum_{k=-\infty}^{+\infty} \hat{u}_{j,k}\, w_{j,k}(x). \tag{3}$$

Here the wavelet transform $\hat{u}_{j,k}$ and the scaling-function transform $\bar{u}_{J,k}$ are, respectively, the inner products of $u(x)$ with $w_{j,k}(x)$ and $s_{J,k}(x)$. The transformation (1)–(3) is defined for the individual wavelets (see below), which offer different representations of the same signal.

Wavelets make trade-offs between how compactly they are localized in the space regime and in the wavenumber regime. The wavelet of Haar (1910) is an extreme example, which is a sharp pulse in space and thus poorly concentrated in wavenumber:

$$w(x) = \begin{cases} +1 & \text{for } 0 \leqslant x < \frac{1}{2} \\ -1 & \text{for } \frac{1}{2} \leqslant x < 1 \\ 0 & \text{elsewhere,} \end{cases} \tag{4}$$

$$s(x) = \begin{cases} +1 & \text{for } 0 \leqslant x < 1 \\ 0 & \text{elsewhere.} \end{cases} \tag{5}$$

We have Harmonic wavelets at the opposite side of the uncertainty principle (Newland 1993; Mouri & Kubotani 1995):

$$w(x) = \frac{\sin(2\pi x + \varphi) - \sin(\pi x + \varphi)}{\pi x} \quad (0 \leqslant \varphi \leqslant \pi/2), \tag{6}$$

$$s(x) = \frac{\sin(\pi x)}{\pi x}. \tag{7}$$

The parameter φ determines the shape of the mother wavelet. The other types of wavelets are intermediate between these two extremes.

2.2. *Implementation of wavelets*

Practical applications of wavelets require discrete transformations. This is because a function $u(x)$ is sampled as a sequence $u[n] = u(n\Delta)$, where Δ denotes the sampling interval. The length of the input signal is required to be a power of 2 ($n = 0$ to $2^N - 1$). We assume that the signal and the basis functions are periodic with a period of 2^N. Then the reconstruction formula (3) is replaced by

$$u[n] = \sum_{k=0}^{2^J-1} \bar{u}_{J,k}\, s_{J,k}[n] + \sum_{j=J}^{N-1} \sum_{k=0}^{2^j-1} \hat{u}_{j,k}\, w_{j,k}[n] \quad (1 \leqslant J \leqslant N-1). \tag{8}$$

Here the basis functions remain complete and orthonormal.

Figure 1 shows examples of wavelets (solid lines) and scaling functions (dotted lines) for $N = 13$, $j = J = 9$, and $k = 256$ (left panels). Their power spectra in the wavenumber domain are also illustrated (right panels). We have already mentioned Haar's and Harmonic wavelets defined on the real line. The general forms of discrete Haar's base are

$$w_{j,k}[n] = \begin{cases} +2^{-(N-j)/2} & \text{for } n = 2^{N-j}k \text{ to } 2^{N-j}k + 2^{N-j-1} - 1 \\ -2^{-(N-j)/2} & \text{for } n = 2^{N-j}k + 2^{N-j-1} \text{ to } 2^{N-j}(k+1) - 1 \\ 0 & \text{elsewhere,} \end{cases} \tag{9}$$

$$s_{J,k}[n] = \begin{cases} +2^{-(N-J)/2} & \text{for } n = 2^{N-J}k \text{ to } 2^{N-J}(k+1) - 1 \\ 0 & \text{elsewhere.} \end{cases} \tag{10}$$

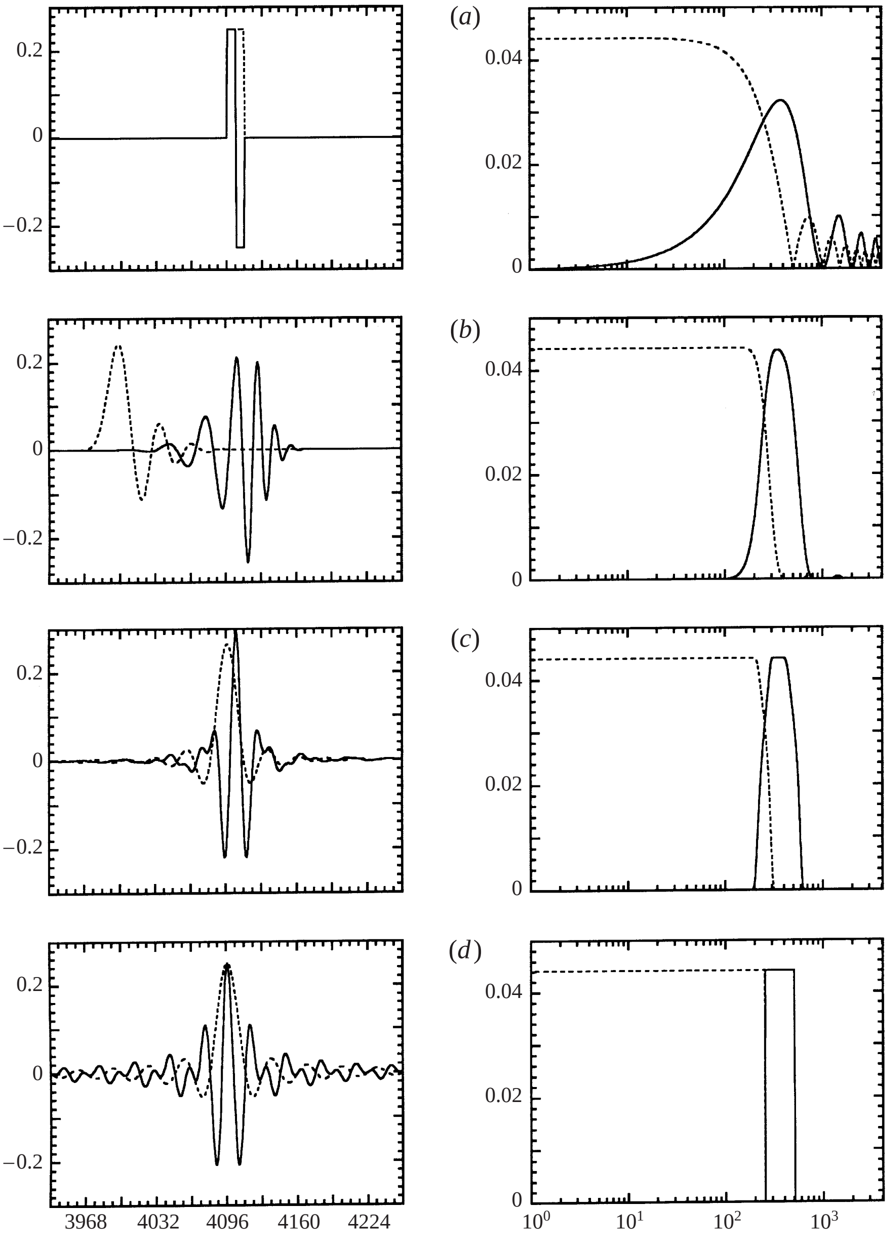

FIGURE 1. Wavelets (solid lines) and scaling functions (dotted lines) with $N = 13$, $j = J = 9$, and $k = 256$: (*a*) Haar's (*b*) Daubechies' 20-tap, (*c*) Meyer's, and (*d*) Harmonic ($\varphi = 0$). Their power spectra in the wavenumber domain are shown in the right column. The spectra of the Harmonic base are computed from the scalar products with $\exp(\mathrm{i}2\pi(m + 1/2)n/2^N)$, instead of the usual $\exp(\mathrm{i}2\pi mn/2^N)$, where m is the wavenumber (Appendix A).

The 20-tap wavelet of Daubechies (1988) is another function that is compact in space. It is more localized in wavenumber than Haar's. The wavelet of Meyer (1985–1986) is compact in wavenumber. It is more localized in space than Harmonic wavelets. These four types of bases are used in our analyses to follow. The numerical algorithms are from Strang (1989), Press *et al.* (1992), Yamada & Ohkitani (1991), and Mouri & Kubotani (1995, see also Appendix A).

2.3. *Meaning of wavelet transforms*

The space–scale localization and the zero average indicate that a wavelet $w_{j,k}[n]$ extracts signal variations of the scale 2^{N-j-1} around the point $n = 2^{N-j}k$ (Yamada & Ohkitani 1991; Meneveau 1991). For example, the Haar-wavelet transform $\hat{u}_{j,0}$ is given by

$$\hat{u}_{j,0} = 2^{-(N-j)/2}(u[0] + \cdots + u[2^{N-j-1} - 1] - u[2^{N-j-1}] - \cdots - u[2^{N-j} - 1]). \quad (11)$$

The product $2^{(j+2-N)/2}\hat{u}_{j,0}$ is equal to the average of the differences $u[n] - u[n + 2^{N-j-1}]$ with $n = 0$ to $2^{N-j-1} - 1$. Thus wavelet transforms of velocities are analogous to velocity increments:

$$|u(x+\delta) - u(x)| \sim 2^{(j+2-N)/2}|\hat{u}_{j,k}|, \quad (12)$$

with

$$x \sim 2^{N-j}k\Delta \quad \text{and} \quad \delta \sim 2^{\mathrm{N-j-1}}\Delta. \quad (13)$$

There are two fundamental differences. First, increments are determined by variations of scale δ or less, while wavelet transforms are concentrated on given scales. Second, except for Haar's base, wavelets oscillate many times so that the signs of the transforms are of no physical interest.

We base our analyses on moments of wavelet transforms. The signal is divided into M segments of 2^N points. To each of them, the wavelet transformation is applied. The wavelet moment for a certain scale is obtained by averaging over all the segments and k-locations:

$$\langle \hat{u}^q \rangle_j = \frac{1}{M}\frac{1}{2^j}\sum_{m=1}^{M}\sum_{k=0}^{2^j-1}\hat{u}^q_{m,j,k} \quad (q \in Z^+, 1 \leqslant j \leqslant N-1). \quad (14)$$

Here m indicates that the transform belongs to the mth segment. The first-order moment is the average. When $u[n]$ is a random signal, $\langle \hat{u} \rangle_j$ converges to zero at large M. The second-order moment is related to the energy; $\hat{u}^2_{m,j,k}$ provides the local energy of a given scale at a given position, and $2^j\langle \hat{u}^2 \rangle_j$ provides the total energy of the scale. In general, a wavelet moment of an even order corresponds to the 'structure function', i.e. moment of velocity increments, at the same order:

$$\langle \hat{u}^q \rangle_j \sim 2^{(N-j-2)q/2}\langle (u(x+\delta) - u(x))^q \rangle \quad (q/2 \in Z^+). \quad (15)$$

Here $\langle\ \rangle$ means the spatial average. For another character of wavelet transforms, see Appendix B.

2.4. *Removal of end effects*

Except for the case of Haar's base, it follows from the periodic boundary condition that some wavelet transforms at each scale are affected by data from both ends of the input signal. The discontinuity between the signal ends could be mistaken as a structure, especially at small scales. This end effect is removed by adding half-lengths of data to each end before performing the transformation (Meneveau 1991). When we are interested in a signal segment $u_m[n]$ from $n = 0$ to $2^N - 1$, we consider in addition the adjacent segments on both sides, forming a new segment of length 2^{N+1}, as illustrated in figure 2:

$$u'_m[n'] = \begin{cases} u_{m-1}[n' + 2^{N-1}] & \text{for } n' = 0 \text{ to } 2^{N-1} - 1 \\ u_m[n' - 2^{N-1}] & \text{for } n' = 2^{N-1} \text{ to } 2^{N-1} + 2^N - 1 \\ u_{m+1}[n' - 2^{N-1} - 2^N] & \text{for } n' = 2^{N-1} + 2^N \text{ to } 2^{N+1} - 1. \end{cases} \quad (16)$$

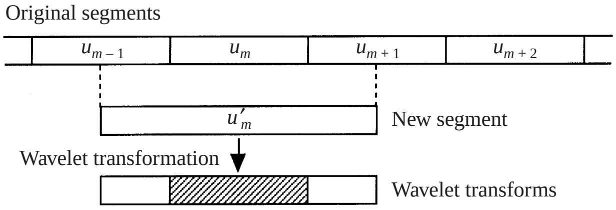

FIGURE 2. Schematic representation of our method to remove the end effect.

The wavelet transforms are obtained for $j' = 1$ to N and $k' = 0$ to $2^{j'}-1$. However, the subsequent analyses are restricted to the original scales and positions: $j = j' - 1 = 1$ to $N - 1$ and $k = k' - 2^{j'-2} = 0$ to $2^j - 1$. In our following studies, the end effect is no longer serious. This fact has been ascertained by increasing and decreasing the numbers of the transforms analysed.

3. Experiment

The experiment was done in the wind tunnel of Meteorological Research Institute. The test section of the tunnel is 3 m × 2 m in cross-section and 18 m in length. Turbulence was produced by placing a biplane grid across the entrance to the test section. The grid consisted of two layers of uniformly spaced rods, the axes of which were perpendicular to each other. The rods were 4 cm × 4 cm in cross-section. The axes of the adjacent rods were separated by 20 cm. The turbulent flow is anisotropic at scales > 1 m. This is mainly due to the limitation of the size of the wind tunnel. In addition, the oriented and inhomogeneous character of the largest-scale flow at the grid position persists downstream. Nevertheless, at the smaller scales, the turbulence is expected to be isotropic.

The longitudinal ($U + u$) and transverse (v) velocities were measured with a hot-wire anemometer. Here U is the average while u and v are the fluctuations. The anemometer was composed of a crossed-wire probe (Dantec, 55P54) and a constant-temperature system (Dantec, Model 5600). The probe was positioned on the tunnel axis at 3 m downstream of the grid. The hot wires were platinum-coated tungsten filaments, 5 µm in diameter, 1.25 mm in length, 1.25 mm in separation, and oriented at $\pm 45°$ to the mean-flow direction. Pitch-angle calibration was done in the tunnel before the experiment. The signals were recorded at an interval of 150 µs, after low-pass filtering at 7 kHz (Krohn-Hite, Model 3322, 24 dB/octave) and digitized with 12-bit resolution (Canopus, ADXM-98L).† The analog filter was used to remove the spike noise, which was due to electromagnetic pulses from the motor of the wind tunnel. The entire length of the signals was long ($\sim 10^7$ points), because we need to minimize the statistical uncertainties.

The turbulence level, expressed by the ratio of the root-mean-square value of the longitudinal fluctuation ($\langle u^2 \rangle^{1/2} = 0.54\,\mathrm{m\,s^{-1}}$) to the mean longitudinal velocity ($U = 8.65\,\mathrm{m\,s^{-1}}$), was as small as 0.06. Hence we base the following analyses on the frozen-eddy hypothesis of Taylor (1938), $\partial/\partial t = -U\partial/\partial x$, which converts temporal

---

† To avoid aliasing, the sampling frequency has to be at least twice of the highest frequency present in the analog signal, i.e. the cutoff frequency of the analog filter. This requirement was not satisfied. Nevertheless, in practice, the aliasing does not affect our analyses. The energy spectra in figure 3 go towards zero as the frequency approaches the sampling frequency. If the aliasing were significant, the spectra would go towards some non-zero value.

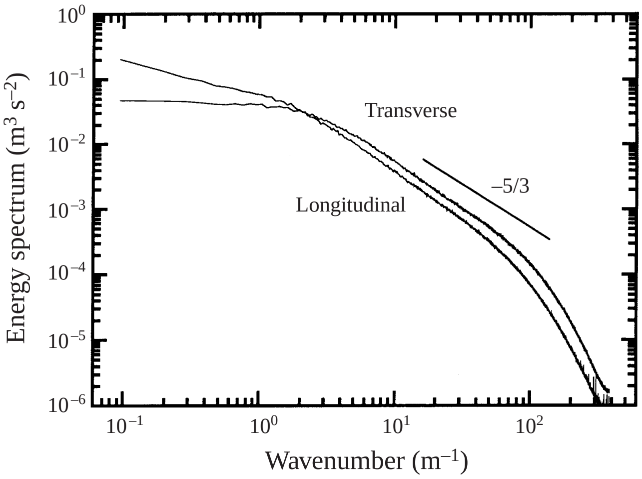

FIGURE 3. Energy spectra of the turbulent flow behind the grid. These are obtained by averaging over 1200 segments of the data, each of which is made of a series of 8192 points. We indicate the $-5/3$ power law of Kolmogorov's spectrum. The wavenumber is in m^{-1}, instead of usual radian m^{-1}.

Mean velocity at hot wire location	$U = 8.65\,\mathrm{m\,s^{-1}}$
R.m.s. velocity fluctuation (longitudinal)	$\langle u^2\rangle^{1/2} = 0.54\,\mathrm{m\,s^{-1}}$
R.m.s. velocity fluctuation (transverse)	$\langle v^2\rangle^{1/2} = 0.52\,\mathrm{m\,s^{-1}}$
Kinematic viscosity	$\nu = 0.0000141\,\mathrm{m^2\,s^{-1}}$
Mean energy dissipation rate	$\langle\varepsilon\rangle = 15\nu\langle(\partial u/\partial x)^2\rangle = 0.99\,\mathrm{m^2\,s^{-3}}$
Integral length	$L = \int\langle u(x+\delta)u(x)\rangle/\langle u^2\rangle \mathrm{d}\delta = 0.24\,\mathrm{m}$
Taylor microscale	$\lambda = (\langle u^2\rangle/\langle(\partial u/\partial x)^2\rangle)^{1/2} = 0.0079\,\mathrm{m}$
Kolmogorov length	$\eta = (\nu^3/\langle\varepsilon\rangle)^{1/4} = 0.00023\,\mathrm{m}$
Reynolds number	$Re_\lambda = \langle u^2\rangle^{1/2}\lambda/\nu = 300$
Inertial range	$\delta_i = 0.008$–$0.016\,\mathrm{m}$
Sampling interval	$\Delta = 0.00015$ s
Number of points	$M \times 2^N = 1200 \times 8192$

TABLE 1. Summary of experimental conditions. The scales are all in the mean-flow direction. The ranges of the measured fluctuations are $-2.49\,\mathrm{m\,s^{-1}} \leqslant u \leqslant 3.06\,\mathrm{m\,s^{-1}}$ and $-2.92\,\mathrm{m\,s^{-1}} \leqslant v \leqslant 3.36\,\mathrm{m\,s^{-1}}$.

variations into spatial variations in the mean-wind direction. The applicability of Taylor's hypothesis has been summarized in Champagne (1978).

We compute the energy spectra in the wavenumber domain, by averaging over 1200 segments of the data, each of which is made of a time series of 8192 points. The spectra are illustrated in figure 3. A straight line denotes the $-5/3$ power law, i.e. Kolmogorov's spectrum for the inertial range. From the spectra, it is evident that the energy-containing, inertial, and dissipation ranges are all captured. We also compute the flow parameters such as the integral length L, the Kolmogorov length η, the Taylor microscale λ, and the Reynolds number Re_λ. The results are listed in table 1. The inertial range there has been defined in the space domain (Kolmogorov 1941*b*). That is, if δ_i lies in the inertial range, we have

$$\langle (u(x+\delta_i) - u(x))^3\rangle = -\tfrac{4}{5}\delta_i\langle\varepsilon\rangle. \tag{17}$$

Here $\langle\varepsilon\rangle$ is the spatial average of the energy dissipation rate. The range determined from (17) is narrower than that inferred from the energy spectra, as has been reported in the previous studies (Anselmet *et al.* 1984).

4. Results

The experimental data are analysed with five families of wavelets: Haar's, Daubechies', Meyer's, symmetric Harmonic ($\varphi = 0$), and anti-symmetric Harmonic ($\varphi = \pi/2$). The mean velocity U is subtracted from the original signal, and the signal is divided into 1200 segments of 8192 points ($M = 1200$, $N = 13$). Wavelet transformations are applied to each segment. Moments of the transforms are averaged over the segments. We first address convergence of the moments, and then use the moments to investigate the turbulence. The velocity increments are also calculated. Their results are, if possible, compared with those of the wavelet transforms.

4.1. *Convergence of wavelet moments*

Higher moments give more weight to the tail of the distribution. If the tail is to be properly determined, long data are required. To test convergence of the wavelet moments, we plot (14) as a function of the total number of segments, from $M = 1$ to 1200 (Anselmet *et al.* 1984). Figure 4 illustrates the second- and fourth-order moments of the longitudinal component for Meyer's wavelet at the scale of $j = 9$ (solid lines), together with the structure functions over the corresponding scale (dotted lines). They are normalized by the final values at $M = 1200$. Wavelet moments and structure functions exhibit a number of oscillations, being approximately in phase. With an increase of the data length, the amplitudes decrease to within 1% of the final values. Hence statistical uncertainties are less than 1% at $M = 1200$. We also observe in figure 4 that convergence is more rapid for second-order moments and for structure functions than it is for fourth-order moments and for wavelet moments.

The same test has been applied to all the wavelet moments used in this study. The results are insensitive to the choice of wavelet. However, the convergence depends on the scale. This is because (i) the total number of transforms $2^j M$ becomes large as the scale index j is increased, and (ii) the turbulent signal is intermittent at small scales. The fourth-order moments are uncertain by 5–10% at the largest scale ($j = 1$), 1–2% at the integral-length scale ($j \simeq 5$), $\leqslant$ 1% at the inertial-range scales ($j \simeq 9$), and 1–2% at the smallest scale ($j = 12$). On the other hand, the statistical uncertainties of the second-order moments are less than 1% throughout the scales. This is due to the rapid convergence of the second-order moments.

4.2. *Flatness factor*

The magnitude of spatial fluctuations of the wavelet transforms is studied at each scale. We use the so-called flatness factor:

$$\text{flatness factor} = \frac{\langle \hat{u}^4 \rangle_j}{\langle \hat{u}^2 \rangle_j^2}. \tag{18}$$

The flatness factor represents the peakedness or flatness of the probability distribution. When the distribution is a Gaussian, the flatness factor is equal to 3. A higher value means that the tail of the distribution is more pronounced than that of a Gaussian. Thus the flatness factor grows as the distribution becomes more intermittent.

Figure 5 illustrates the flatness factor for the longitudinal (filled circles) and transverse (open circles) components as a function of the wavelet scale δ. The scale is

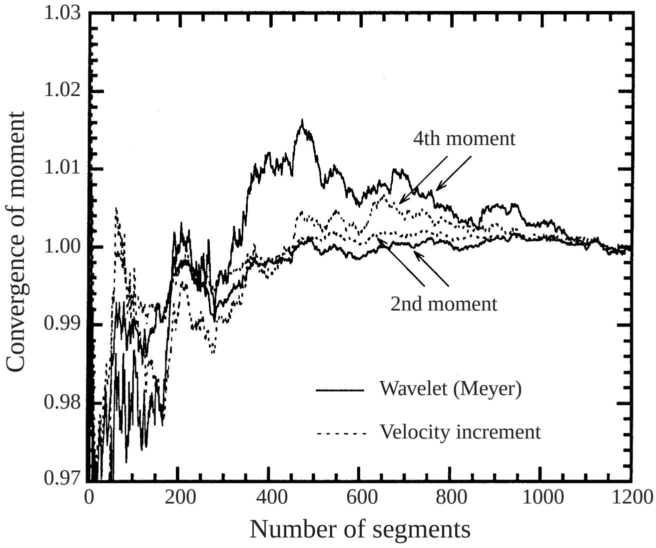

FIGURE 4. Convergence of wavelet moments (solid lines) and structure functions (dotted lines) to their values at the maximum record length. Second- and fourth-order moments are illustrated. Wavelet moments are computed with (14) for Meyer's wavelet at $j = 9$ ($M = 1$–1200, $N = 13$). The longitudinal component of the laboratory data is used.

computed from (13) and normalized by the Kolmogorov length η. The integral length L, the Taylor microscale λ, and the inertial-range limits are indicated.

The scale dependence of the flatness factor is evident in figure 5. At large scales, it is equal to the Gaussian value of 3. As the scale is decreased below the integral length, the flatness factor begins to increase. Around the Taylor microscale, the increase becomes significant. Thus the spatial distribution of $\hat{u}_{j,k}$ is progressively intermittent. The transverse component yields a higher flatness factor than the longitudinal component at all the scales that are below the integral length. For a longitudinal component, similar features were observed by Meneveau (1991).

There is agreement in figure 5 between different wavelets at this level of description. However, the significant increase below the Taylor microscale is unclear in the case of Haar's wavelet (figure 5*a*). Compared with the flatness factors for the other wavelets, that for Haar's wavelet is high at the Taylor microscale and low at the smaller scales. We consider that the poor localization of Haar's wavelet in the wavenumber regime (figure 1*a*) has caused some leakage of information among the scales.

Figure 5(*a*) also shows the flatness factor of the velocity increments (solid lines), which agrees well with the flatness factor of Haar's transforms. This agreement supports the analogy (12)–(13). We have stated in § 2.3 that increments reflect variations of scale δ or less. When $\delta \leqslant L$, however, velocity variations of the smaller scales hold less energy than those of the larger scales, and the major contribution to the increments comes from variations of scales comparable with δ.

Since the enhancement of the flatness factor is due to the enhanced tail of the probability distribution, the energies at small scales are expected to be dominated by a small number of the wavelet transforms. To demonstrate this, for each of the scales, we compute the number fractions of wavelet transforms with $\hat{u}^2_{j,k} > \langle \hat{u}^2 \rangle_j$ and $\hat{u}^2_{j,k} > 2\langle \hat{u}^2 \rangle_j$. These wavelet transforms contribute significantly to the scale energies. The results are illustrated in figure 6. We have used Meyer's wavelet. Dotted lines

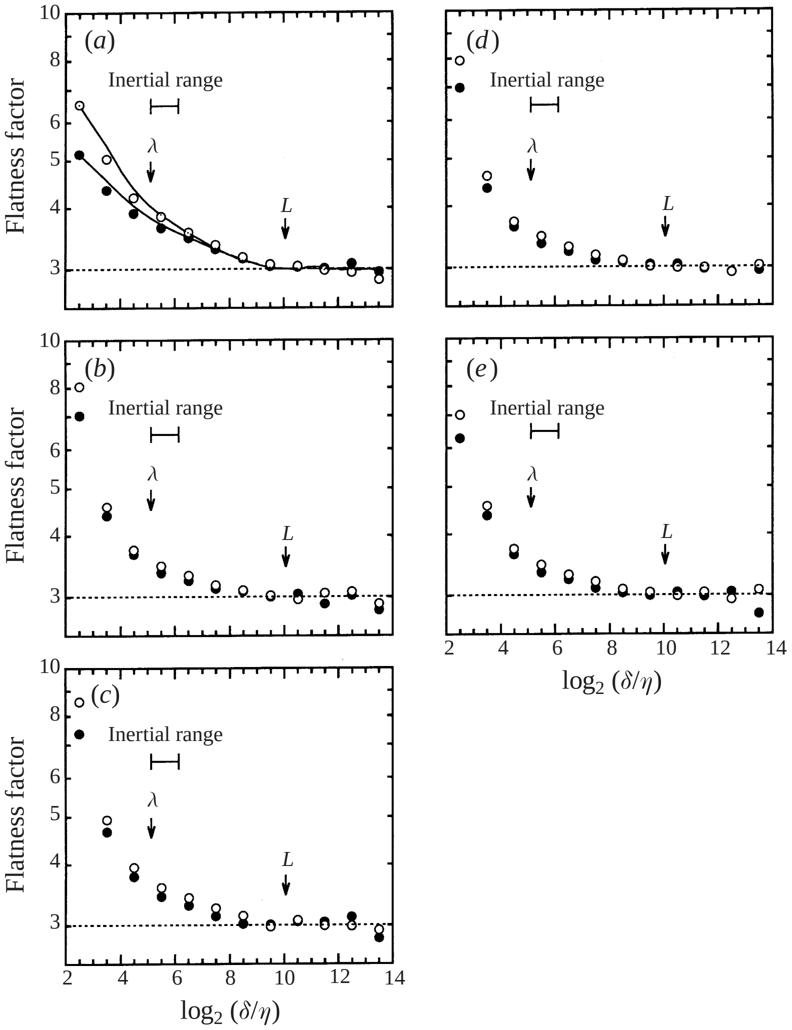

FIGURE 5. Flatness factor versus wavelet scale. The bases used are (*a*) Haar's, (*b*) Daubechies', (*c*) Meyer's, (*d*) Harmonic with $\varphi = 0$, and (*e*) Harmonic with $\varphi = \pi/2$. The flatness factor is obtained with (18) from the laboratory data ($M = 1200$, $N = 13$). The wavelet scale δ is defined in (13) and normalized by the Kolmogorov length η. Filled circles are for the longitudinal component. Open circles are for the transverse component. Solid lines denote the flatness factor of the velocity increments. We indicate the integral length L, the Taylor microscale λ, and the inertial range limits.

indicate the values expected for a Gaussian. With decreasing the scale, the number fractions are in fact decreased from the Gaussian values.

4.3. *Scale–scale correlation*

Orthonormal wavelets provide a unique opportunity to investigate a correlation in space between variations of different scales. We explore the correlation of squared wavelet transforms, i.e. local energies, between the adjacent scales of $j-1$ and j. Though the extents of $w_{j-1,k}[n]$ and $w_{j,k}[n]$ in space are different, those of $s_{j,k}[n]$ and $w_{j,k}[n]$ are identical (figure 1). Hence the wavelet transforms at the scale of $j-1$ are

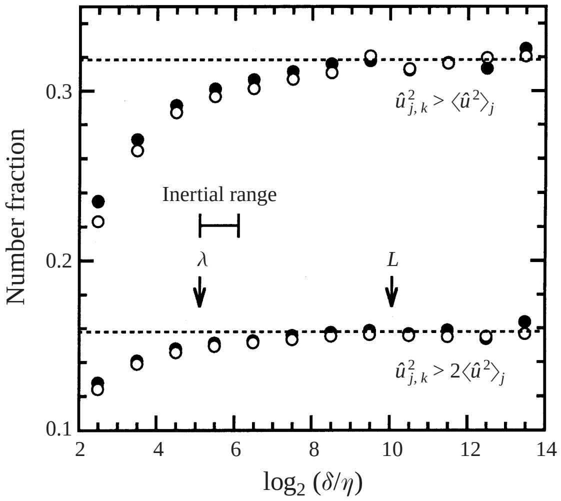

FIGURE 6. Number fractions of wavelet transforms with $\hat{u}^2_{j,k} > \langle \hat{u}^2 \rangle_j$ and $\hat{u}^2_{j,k} > 2\langle \hat{u}^2 \rangle_j$. We have analysed the laboratory data with Meyer's wavelet ($M = 1200$, $N = 13$). Filled circles are for the longitudinal component. Open circles are for the transverse component. Dotted lines indicate the values expected for a Gaussian.

converted into the scaling-function transforms at the scale of j for each segment:

$$\bar{u}'_{m,j,k} = \sum_{n=0}^{2^N-1} \sum_{k'=0}^{2^{j-1}-1} s_{j,k}[n]^* \, \hat{u}_{m,j-1,k'} \, w_{j-1,k'}[n]$$

$$(1 \leqslant m \leqslant M,\ 2 \leqslant j \leqslant N-1,\ 0 \leqslant k \leqslant 2^j - 1). \quad (19)$$

Here $*$ denotes complex conjugate. The sum over k' is to construct a signal from the wavelet transforms, and the sum over n is to expand the signal into the scaling-function transforms. Then we calculate Pearson's correlation coefficient between $\hat{u}^2_{m,j,k}$ and $\bar{u}'^2_{m,j,k}$:

$$R = \frac{\langle \hat{u}^2 \bar{u}'^2 \rangle_j - \langle \hat{u}^2 \rangle_j \langle \bar{u}'^2 \rangle_j}{(\langle \hat{u}^4 \rangle_j - \langle \hat{u}^2 \rangle_j^2)^{1/2} (\langle \bar{u}'^4 \rangle_j - \langle \bar{u}'^2 \rangle_j^2)^{1/2}}. \quad (20)$$

Here moments are defined as in (14). For instance,

$$\langle \hat{u}^2 \bar{u}'^2 \rangle_j = \frac{1}{M} \frac{1}{2^j} \sum_{m=1}^{M} \sum_{k=0}^{2^j-1} \hat{u}^2_{m,j,k} \, \bar{u}'^2_{m,j,k}. \quad (21)$$

The value of R ranges from 0, if there is no correlation, to ±1, if there is a linear correlation. The sign of R depends on the trend for the values of one quantity to increase ($R > 0$) or decrease ($R < 0$) on increasing the other.

Figure 7 illustrates the correlation between the adjacent scales of $j-1$ and j for the longitudinal (filled circles) and transverse (open circles) components of our grid turbulence, as a function of the scale of j. Symbols are the same as in figure 5. We have employed Meyer's and Harmonic bases. The other bases are of no use. Daubechies' wavelets do not overlap the scaling functions with the same values of j and k in space (figure 1*b*). Haar's base has turned out to introduce spurious scale–scale correlations for an artificial random signal (Appendix C). We have ascertained that Meyer's and Harmonic bases give zero coefficients for the random signal.

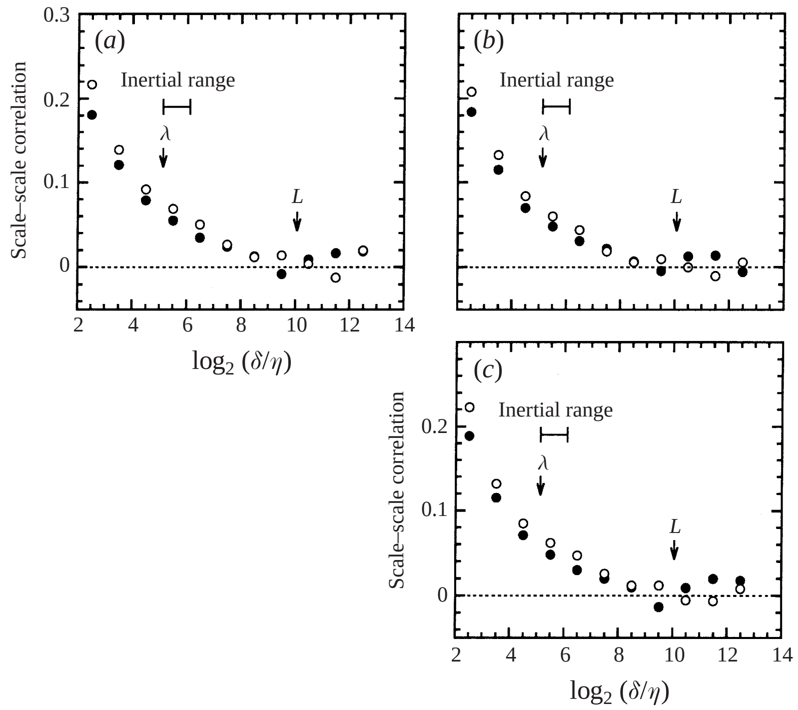

FIGURE 7. Scale–scale correlation versus wavelet scale. The bases used are (*a*) Meyer's, (*b*) Harmonic with $\varphi = 0$, and (*c*) Harmonic with $\varphi = \pi/2$. The correlation coefficient is obtained with (20) from the laboratory data ($M = 1200$, $N = 13$). Filled circles are for the longitudinal component. Open circles are for the transverse component.

The scale–scale correlation in figure 7 is absent at large scales, and increases as the scale is decreased below the integral length L. The increase becomes significant around the Taylor microscale λ. The scale–scale correlation at small scales is better in the transverse velocity than in the longitudinal velocity. These features are the same for all the wavelets. Yamada & Ohkitani (1991) obtained a similar result for a longitudinal component, by using a different diagnostic of scale–scale correlation.

We have also studied the correlation between the scales of $j-2$ and j as well as the correlation between the scales of $j-3$ and j in the same manner (not shown here). Their dependences on j are similar to that of the correlation between the scales of $j-1$ and j. The transverse velocity yields better correlations than the longitudinal velocity at small scales. With increasing the distance in scale, the scale–scale correlation becomes less significant at all the j values.

4.4. *Longitudinal–transverse correlation*

The correlation between wavelet transforms of the longitudinal (u) and transverse (v) components is studied in space at each of the scales. We again resort to the correlation coefficient:

$$R = \frac{\langle \hat{u}^2 \hat{v}^2 \rangle_j - \langle \hat{u}^2 \rangle_j \langle \hat{v}^2 \rangle_j}{(\langle \hat{u}^4 \rangle_j - \langle \hat{u}^2 \rangle_j^2)^{1/2} (\langle \hat{v}^4 \rangle_j - \langle \hat{v}^2 \rangle_j^2)^{1/2}}, \tag{22}$$

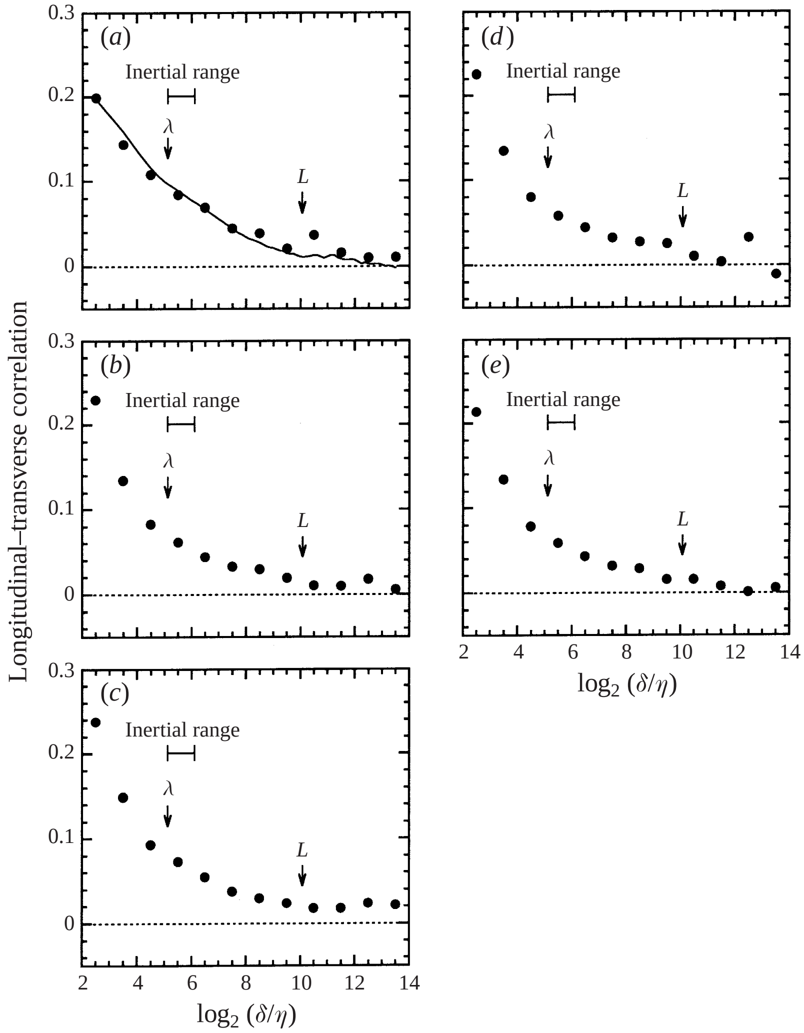

FIGURE 8. Longitudinal–transverse correlation versus wavelet scale. The bases used are (*a*) Haar's, (*b*) Daubechies', (*c*) Meyer's, (*d*) Harmonic with $\varphi = 0$, and (*e*) Harmonic with $\varphi = \pi/2$. The correlation coefficient is obtained with (22) from the laboratory data ($M = 1200$, $N = 13$). A solid line denotes the correlation of the velocity increments.

where

$$\langle \hat{u}^2 \hat{v}^2 \rangle_j = \frac{1}{M}\frac{1}{2^j}\sum_{m=1}^{M}\sum_{k=0}^{2^j-1} \hat{u}^2_{m,j,k}\,\hat{v}^2_{m,j,k}, \tag{23}$$

and so on. The results are illustrated in figure 8 (filled circles). We also plot the longitudinal–transverse correlation computed from the velocity increments (solid line), which is in agreement with the correlation of Haar's transforms. The other symbols are the same as in figure 5.

The longitudinal–transverse correlation in figure 8 has nearly the same dependence on scales as the scale–scale correlation in figure 7. At large scales, the longitudinal–transverse correlation is absent. As the scale is decreased below the integral length L, the longitudinal–transverse correlation begins to increase. Around the Taylor microscale λ, the increase becomes significant. The overall trends in figure 8 are essentially the same for all the wavelets. However, the rapid increase below the Taylor microscale is unclear in Haar's transforms, and in the velocity increments as well (figure 8*a*). A plausible explanation is that Haar's wavelets and increments are not so localized in the wavenumber regime (see § 4.2).

5. Comparison with numerical and analytic models

Our wavelet analyses of laboratory turbulence have demonstrated the existence of structures in the velocity field. On the other hand, direct numerical simulations (Jiménez *et al.* 1993), bubble-visualization experiments (Douady, Couder & Brachet 1991), and large-Reynolds-number asymptotics (Moffatt, Kida & Ohkitani 1994) have already established that turbulence includes structures of vorticity ω and dissipation rate ε:

$$\omega = \left(\left(\frac{\partial u_2}{\partial x_3} - \frac{\partial u_3}{\partial x_2} \right)^2 + \left(\frac{\partial u_3}{\partial x_1} - \frac{\partial u_1}{\partial x_3} \right)^2 + \left(\frac{\partial u_1}{\partial x_2} - \frac{\partial u_2}{\partial x_1} \right)^2 \right)^{1/2}, \tag{24}$$

and

$$\varepsilon = \frac{\nu}{2} \sum_{m=1}^{3} \sum_{n=1}^{3} \left(\frac{\partial u_m}{\partial x_n} + \frac{\partial u_n}{\partial x_m} \right)^2 . \tag{25}$$

Here subscripts refer to coordinate directions. Regions of intense vorticity are organized into tubes, which occupy a small fraction of the volume. The vortex tubes have radii of the order of the Kolmogorov length. Their lengths are of the order of the integral length. Dissipation is significant around the tubes. These structures are considered to be embedded in a background flow field that is random and uncorrelated (see Nelkin 1994; Frisch 1995; or Sreenivasan & Antonia 1997 for a review).

The effects of these tubes on the velocity fields have not been clarified by the previous analyses on velocity increments. Hence it is of interest to discuss the results of our wavelet analyses in terms of the structures of vorticity and dissipation.† Since reliable measurements of ω and ε in experiments are beyond the reach of the existing techniques, the discussion concerns a flow created by a direct numerical simulation of isotropic turbulence. We also analyse an analytic solution of the Navier–Stokes equation as a model field of the vortex tube.

5.1. *Wavelet analyses of a numerical turbulence*

This section analyses the result of a direct numerical simulation of forced isotropic turbulence. The simulation was done on NEC-SX3 in Osaka University Data Processing Center. We assumed a periodic box. There were 128 grid points in each of the three directions. The forcing was achieved by introducing a negative viscosity coefficient at a low wavenumber. For the time marching, a Runge–Kutta–Gill method was used. The dissipating term of the Navier–Stokes equation was exactly integrated, while the nonlinear term was computed with a pseudo-spectral method. The aliasing was removed by a phase-shifted polyhedral truncation. The truncation wavenumber was roughly twice the Kolmogorov wavenumber. The data to be analysed are taken from a snapshot after the turbulence had settled to a steady state. The basic parameters are listed in table 2. We have ascertained the presence of vortex tubes in the flow.

---

† See Yamada & Ohkitani (1991) and Meneveau (1991) for another approach, i.e. the interpretation of wavelet statistics in the context of 'multifractal'.

Mean energy	$E = \int E(k)\mathrm{d}k = 1.57$
Mean enstrophy	$\Omega = \langle \omega^2 \rangle /2 = 46.0$
R.m.s. velocity fluctuation	$\langle u^2 \rangle^{1/2} = (2E/3)^{1/2} = 1.02$
Kinematic viscosity	$\nu = 0.00977$
Mean energy dissipation rate	$\langle \varepsilon \rangle = 2\nu\Omega = 0.898$
Integral length	$L = (2E/3)^{3/2}/(2\nu\Omega) = 1.19$
Taylor microscale	$\lambda = (5E/\Omega)^{1/2} = 0.413$
Kolmogorov length	$\eta = (\nu^2/(2\Omega))^{1/4} = 0.0319$
Reynolds number	$Re_\lambda = (10/(3\Omega))^{1/2}\, E/\nu = 43.3$
Length of box side	2π
Grid points	128^3

TABLE 2. Numerical flow parameters. The symbols k and $E(k)$ denote the wavenumber and the three-dimensional energy spectrum, respectively. The inertial range does not exist in the present data.

For reference, we also study a random-phase signal that is divergence-free and has the same three-dimensional energy spectrum as the numerical turbulence. Throughout the scales, the random-phase signal has no spatial structures (Appendix C), contrasting with the case of the numerical turbulence.

Both in the numerical turbulence and the random-phase signal, wavelet transforms of velocities are compared with scaling-function transforms of vorticity and dissipation. Namely, variations of velocities at certain scales are compared with averages of vorticity and dissipation over such scales. Haar's base is used.† This is because Haar's scaling-function transforms are exactly equivalent to the averages of the signal (see (10)). The transformations are applied to the data on one-dimensional sections of the flow field.‡ Each section consists of 128 grid points ($N = 7$), and is parallel to the x-, y-, or z-axis. There are 3×128^2 sections in total. Moments of the transforms are averaged over them ($M = 3 \times 128^2$).

First we examine correlations of $\hat{u}^2$ and $\hat{v}^2$ with $\bar{\varpi}$ and $\bar{\varepsilon}$. The correlation coefficients are defined in the same manner as described in §4. For instance,

$$R = \frac{\langle \hat{u}^2 \bar{\varpi} \rangle_j - \langle \hat{u}^2 \rangle_j \langle \bar{\varpi} \rangle_j}{(\langle \hat{u}^4 \rangle_j - \langle \hat{u}^2 \rangle_j^2)^{1/2} (\langle \bar{\varpi}^2 \rangle_j - \langle \bar{\varpi} \rangle_j^2)^{1/2}}, \tag{26}$$

where

$$\langle \hat{u}^2 \bar{\varpi} \rangle_j = \frac{1}{M} \frac{1}{2^j} \sum_{m=1}^{M} \sum_{k=0}^{2^j-1} \hat{u}^2_{m,j,k}\, \bar{\varpi}_{m,j,k}. \tag{27}$$

Figure 9 illustrates the correlations in the numerical turbulence (filled circles) and the random-phase signal (open circles). The abscissa is the wavelet scale δ, which is computed from (13) and normalized by the Kolmogorov length η of the turbulence. The $\hat{u}^2$–$\bar{\varepsilon}$, $\hat{v}^2$–$\bar{\varpi}$, and $\hat{v}^2$–$\bar{\varepsilon}$ correlations exist both in the turbulence and the random-phase signal (figures 9*b*–9*d*). These correlations increase as the scale is decreased,

---

† The present analyses are restricted to the individual scales, and thus free from the drawback that Haar's base introduces spurious scale–scale correlations (Appendix C).

‡ The longitudinal and transverse directions are defined, respectively, as being parallel and perpendicular to the one-dimensional section. Since wavelet transforms are equivalent to signal variations along the section, the difference between longitudinal and transverse components is always important.

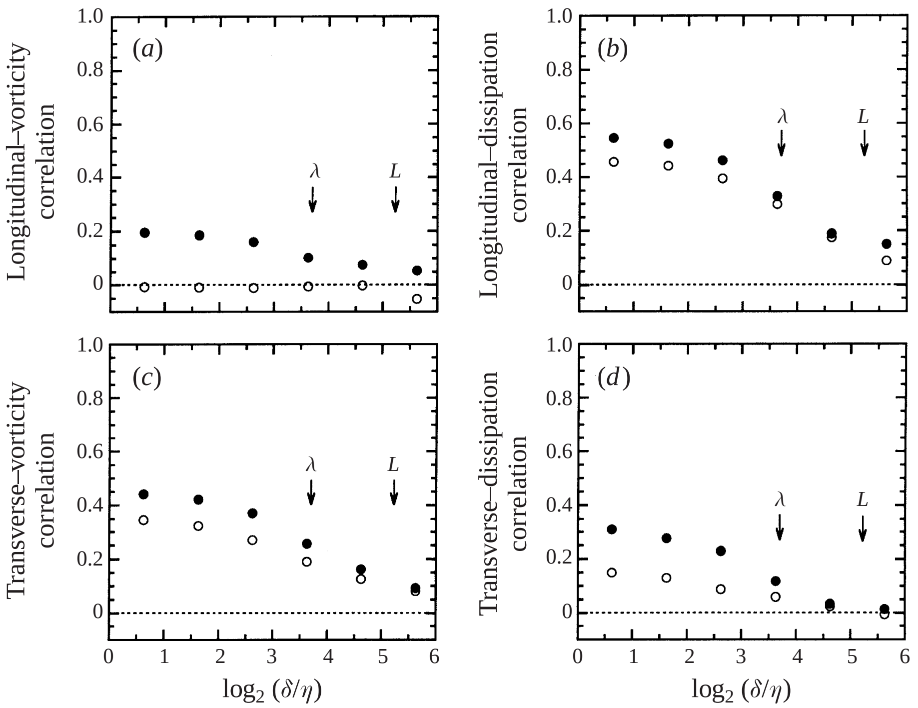

FIGURE 9. Wavelet analyses of the data of the direct numerical simulation (filled circles) and the random-phase signal (open circles): correlations between (*a*) $\hat{u}^2$ and $\bar{\omega}$, (*b*) $\hat{u}^2$ and $\bar{\varepsilon}$, (*c*) $\hat{v}^2$ and $\bar{\omega}$, (*d*) $\hat{v}^2$ and $\bar{\varepsilon}$. Here $\hat{u}$, $\hat{v}$, $\bar{\omega}$, and $\bar{\varepsilon}$ are transforms of longitudinal velocity, transverse velocity, vorticity, and dissipation. The correlation coefficient is obtained with (26) from Haar's transforms ($M = 3 \times 128^2$, $N = 7$). The abscissa is the wavelet scale δ, which is defined in (13) and normalized by the Kolmogorov length η of the numerical turbulence. We indicate the integral length L and the Taylor microscale λ of the numerical turbulence.

especially in the turbulence. On the other hand, the $\hat{u}^2$–$\bar{\omega}$ correlation is present in the turbulence, but entirely absent in the random-phase signal (figure 9*a*).

Next we examine (dimensionless) covariances of $\hat{u}^2$, $\hat{v}^2$, $\hat{u}^4$, and $\hat{v}^4$ with $\bar{\omega}^4$ and $\bar{\varepsilon}^2$. They are defined as, for instance,

$$C = \frac{\langle \hat{u}^2 \bar{\omega}^4 \rangle_j}{\langle \hat{u}^2 \rangle_j \langle \bar{\omega}^4 \rangle_j}. \tag{28}$$

The covariance is enhanced if large values of one quantity are closely associated with large values of the other. Figure 10 illustrates the covariances in the numerical turbulence (filled symbols) and the random-phase signal (open symbols). On decreasing the scale, the covariances in the turbulence become enhanced over those in the random-phase signal. This enhancement is more pronounced in the covariances of $\hat{u}^4$ and $\hat{v}^4$ (circles) than those of $\hat{u}^2$ and $\hat{v}^2$ (squares). We have also found that the enhancement is more pronounced in the covariances with higher powers of $\bar{\omega}$ and $\bar{\varepsilon}$ (not shown here).

The results for the random-phase signal are explained as follows. Wavelet transforms of the longitudinal velocity are large, by definition, in regions of significant longitudinal variations of the longitudinal velocity, where dissipation is strong, as implied in (25) (Kolmogorov 1962). On the other hand, wavelet transforms of the transverse velocity are large in regions of significant longitudinal variations of the

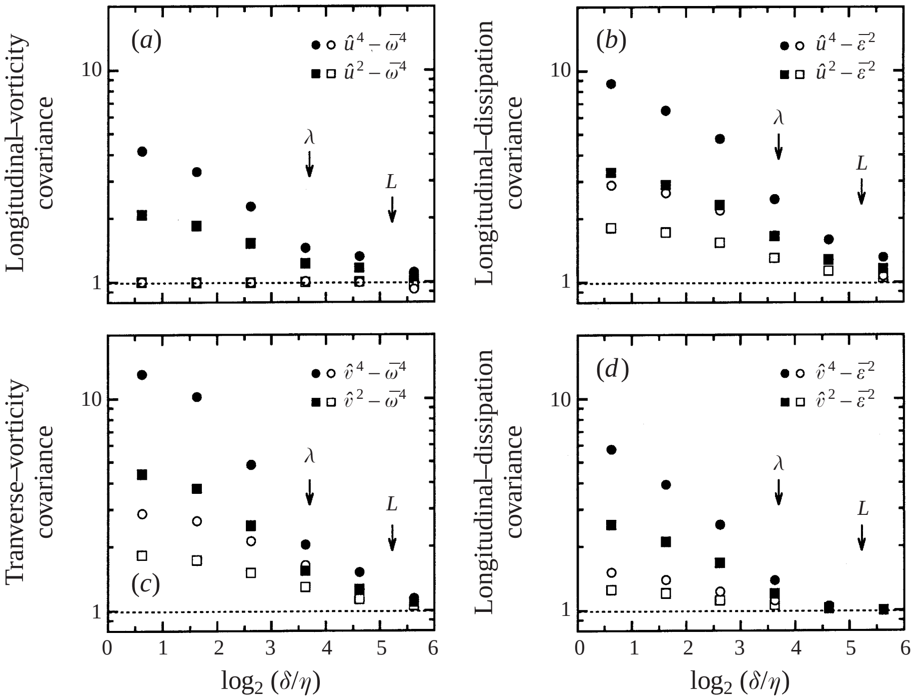

FIGURE 10. Wavelet analyses of the data of the direct numerical simulation (filled symbols) and the random-phase signal (open symbols): covariances between (*a*) $\hat{u}^4$ and $\bar{\omega}^4$, $\hat{u}^2$ and $\bar{\omega}^4$, (*b*) $\hat{u}^4$ and $\bar{\varepsilon}^2$, $\hat{u}^2$ and $\bar{\varepsilon}^2$, (*c*) $\hat{v}^4$ and $\bar{\omega}^4$, $\hat{v}^2$ and $\bar{\omega}^4$, (*d*) $\hat{v}^4$ and $\bar{\varepsilon}^2$, $\hat{v}^2$ and $\bar{\varepsilon}^2$. Here $\hat{u}$, $\hat{v}$, $\bar{\omega}$, and $\bar{\varepsilon}$ are transforms of longitudinal velocity, transverse velocity, vorticity, and dissipation. The covariance is obtained with (28) from Haar's transforms ($M = 3 \times 128^2$, $N = 7$). Circles are for the covariances of $\hat{u}^4$ and $\hat{v}^4$. Squares are for the covariances of $\hat{u}^2$ and $\hat{v}^2$.

transverse velocity, where vorticity is strong, as implied in (24). Such variations also cause some dissipation. With decreasing the scale, Haar's wavelet transforms are increasingly good approximations to the longitudinal derivatives (see (9)), and transforms of velocities are increasingly associated with dissipation and/or vorticity.

The results for the numerical turbulence are different from the results for the random-phase signal. Large values of $\hat{u}$ and $\hat{v}$ are more closely associated with large values of $\bar{\omega}$ and $\bar{\varepsilon}$ in the turbulence than in the random-phase signal. This means that the turbulence has spatial structures where $\hat{u}$, $\hat{v}$, $\bar{\omega}$, and $\bar{\varepsilon}$ are simultaneously enhanced. On the other hand, we have ascertained that vorticity and dissipation of the numerical turbulence are strong in tube-like regions. Therefore, in the turbulence, large values of $\hat{u}$ and $\hat{v}$ are associated with the tubes. In figures 9 and 10, the contribution of those coherent structures is appreciable even above the Taylor microscale λ, and becomes predominant as the scale is decreased.

The Reynolds number for the experiment ($Re_\lambda = 300$) is greater than that for the simulation ($Re_\lambda = 43.3$). Hence, for the numerical turbulence, we study the flatness factor, the number fractions of transforms with $\hat{u}^2_{j,k} > \langle \hat{u}^2 \rangle_j$ and $\hat{u}^2_{j,k} > 2\langle \hat{u}^2 \rangle_j$, the scale–scale correlation, and the longitudinal–transverse correlation. The results are

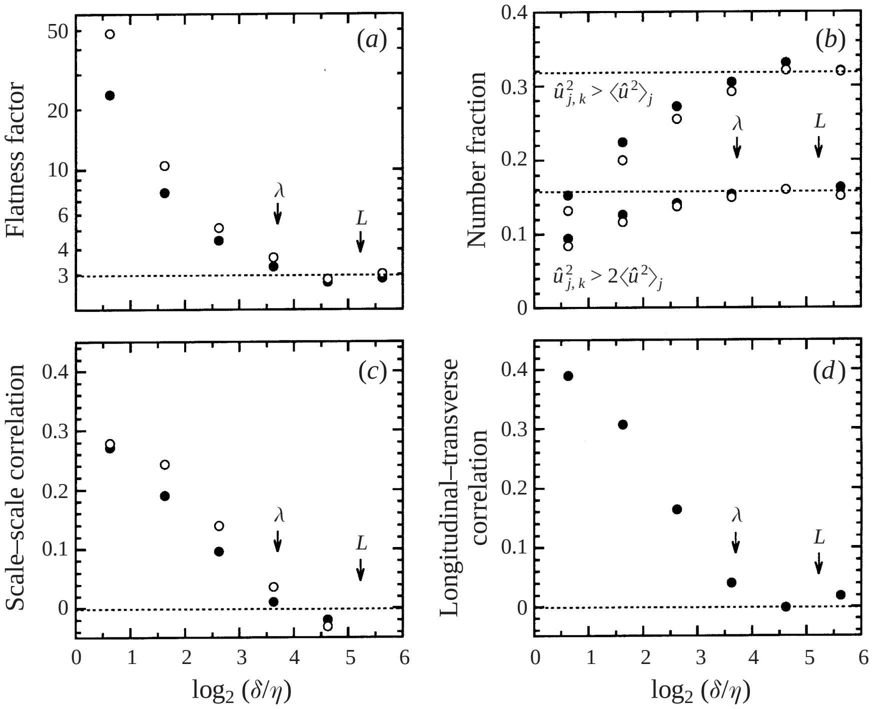

FIGURE 11. Wavelet analyses of the data of the direct numerical simulation: (*a*) flatness factor defined in (18), (*b*) number fractions of wavelet transforms with $\hat{u}^2_{j,k} > \langle \hat{u}^2 \rangle_j$ and $\hat{u}^2_{j,k} > 2\langle \hat{u}^2 \rangle_j$, (*c*) scale–scale correlation defined in (20), and (*d*) longitudinal–transverse correlation defined in (22). We have used Meyer's wavelet ($M = 3 \times 128^2$, $N = 7$). Filled and open circles in (*a–c*) are for the longitudinal and transverse components. Dotted lines indicate the values expected for a Gaussian random field.

illustrated in figure 11. We have used Meyer's wavelet.† Since the data embody the same periodic boundary condition as the wavelet, there is no end effect. The wavelet statistics for the simulation are in rough agreement with those for the experiment (figures 5–8), if we consider the differences in the scale range, the integral length L, and the Taylor microscale λ. Accordingly, when the numerical turbulence is used to interpret our experimental data, the discrepancy in the Reynolds number is ignored (§ 5.3).

5.2. *Wavelet analyses of a model vortex tube*

The present section analyses an axisymmetric solution of the Navier–Stokes equation, which describes a rigid-body rotation for small radii, and a circulation decaying in radius for large radii (Taylor 1918):

$$u_\theta \propto \frac{r}{4\nu^2 t^2} \exp\left(-\frac{r^2}{4\nu t}\right). \tag{29}$$

Here u_θ is the tangential velocity and r is the radius. The velocity is maximal at $r = (2\nu t)^{1/2} = D/2$, as shown in figure 12(*a*). Thus the flow (29) serves as a model

---

† The flatness factor is quite high in the dissipation range. This is due to the compactness of Meyer's wavelet in the wavenumber domain. When Haar's base is used, the flatness factor is relatively low even at the smallest scale: 4.1 for the longitudinal velocity and 5.4 for the transverse velocity. The same trend is also seen in figure 5.

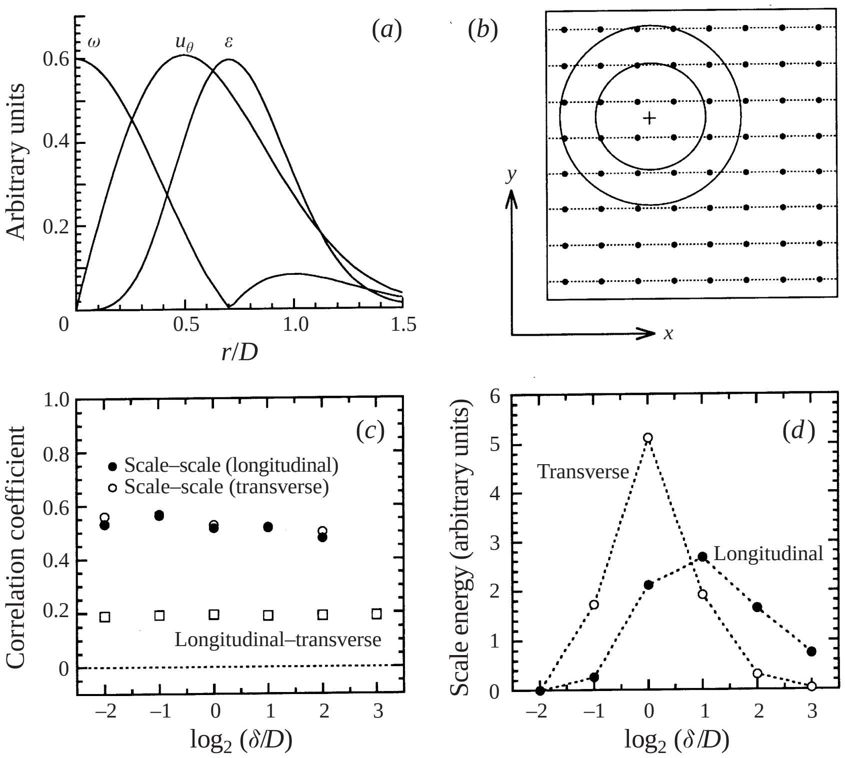

FIGURE 12. Wavelet analyses of the vortex tube (29): (*a*) radial distribution of the tangential velocity u_θ, the vorticity ω, and the dissipation ε, (*b*) configuration of the model field, (*c*) scale–scale correlation defined in (20) and longitudinal–transverse correlation defined in (22), (*d*) total energies of the scales. We have used Meyer's wavelet ($M = 128 \times 500$, $N = 7$). The abscissa in (*c*) and (*d*) is the wavelet scale δ, which is defined in (13) and normalized by the tube diameter D.

for a vortex tube of diameter D. We study the statistics of the wavelet transforms computed on one-dimensional sections across the tube with various distances from its axis.

Figure 12(*b*) shows the configuration considered in our analyses. The tube axis is normal to the (x, y)-plane, and penetrates a square on the (x, y)-plane. The value D is equal to 32^{-1} of the square side. The square is divided into a grid of 128^2 points. There are 128 lines that consist of 128 grid points and are parallel to the x-axis (dotted lines). To the data on the individual lines, Meyer's wavelets are applied ($N = 7$).† This procedure is repeated 500 times, by randomly moving the axis position. Moments of the transforms are averaged over the 128 lines and the 500 repetitions ($M = 128 \times 500$).

Figure 12(*c*) shows the scale–scale and longitudinal–transverse correlations. The abscissa is the wavelet scale δ, which is computed from (13) and normalized by the tube diameter D. Throughout the scales, the scale–scale and longitudinal–transverse correlations are present. Since they are absent in a random and uncorrelated velocity field (Appendix C), we conclude that the scale–scale and longitudinal–transverse correlations emerge only when structures like vortex tubes are contained in the flow.

---

† The velocities have been computed also on points outside the square. These data have been used to remove the end effect (§ 2.4).

Figure 12(*d*) shows the scale energies $2^j\langle\hat{u}^2\rangle_j$ and $2^j\langle\hat{v}^2\rangle_j$. These energies have peaks at $\delta \simeq D$. Vortex tubes contribute mostly to wavelet statistics at the scales that are comparable with their diameters. The longitudinal component has a less pronounced peak at a larger scale. This is because, in our model field (figure 12*a*), the region of intense dissipation, where $\hat{u}^2$ is enhanced, is more extended than the region of intense vorticity, where $\hat{v}^2$ is enhanced. We note that such a geometry is generally seen in the flow fields of vortex tubes that are considered to exist in turbulence (Moffatt *et al.* 1994).

Our conclusion remains valid for a more general situation where the axis of (29) is inclined to the (x, y)-plane. The inclination does not change the form of the velocity signal (Belin *et al.* 1996). However, if the axis is inclined to the x-axis, i.e. the longitudinal direction, the observed size of the tube is greater than its diameter D. Vortex tubes are able to influence the statistics at scales that are as large as their lengths.

5.3. *Interpretation of experimental results*

Now we discuss the implications of the above analyses for our experimental results in figures 5–8. The features at small scales are studied first. Turbulence includes tube-like structures of vorticity and dissipation (Douady *et al.* 1991; Jiménez *et al.* 1993). The presence of the tubes explains the observed enhancements of the flatness factor, the scale–scale, and the longitudinal–transverse correlations. The enhancement of the flatness factor is due to large values of $\hat{u}^4$ and $\hat{v}^4$, which have been shown to be associated with those tubes (§ 5.1). The scale–scale and longitudinal–transverse correlations are enhanced if the statistics are dominated by $\hat{u}$ and $\hat{v}$ at the positions of certain structures (§ 5.2). We have shown that this is the situation in turbulence (§ 5.1). Moreover, the tubes are responsible for substantial fractions of the energies. We have observed that the scale energies are dominated by small numbers of $\hat{u}$ and $\hat{v}$. The large values of these transforms are now attributable to the tubes.

Next we study the experimental results at large scales. The tubes are considered to be embedded in a background flow field that is random, uncorrelated, and mainly of large scales (Jiménez *et al.* 1993). We have observed that the flatness factor is consistent with a Gaussian, and that the scale–scale and longitudinal–transverse correlations are absent. If the central-limit theorem is applied, our results turn out to confirm the random and uncorrelated distribution of the large-scale motions (Appendix C). The flatness factor and the correlation coefficients begin to increase as the scale is decreased from the integral length. This increase is explained by the progressive contribution of the tubes (§ 5.1).

The tubes contribute mostly to the wavelet statistics at scales that are comparable with their sizes in the longitudinal direction, i.e. from their diameters to their lengths (§ 5.2). The diameters and lengths of the tubes are surely of some ranges. Judging from our experimental results, the minimum diameter could be down to the order of the Kolmogorov length, while the maximum length could be up to the order of the integral length. These estimates are consistent with the previous ones (Douady *et al.* 1991; Jiménez *et al.* 1993).

We also present our speculation on the observed tendency that the longitudinal velocity yields a lower flatness factor and a poorer scale–scale correlation than the transverse velocity. The contribution of a vortex tube to the wavelet energies at around the scale of its (observed) size is less pronounced in the longitudinal velocity than in the transverse velocity (§ 5.2). Therefore, for the longitudinal velocity, the effects of the individual tubes might be more liable to be diluted by the background random field, which could contribute, more or less, to the energies at all the scales.

6. Concluding remarks

The structure of turbulence has been studied by using orthonormal wavelets. We have measured longitudinal and transverse velocities of a flow behind a grid, and examined the flatness factor, the scale–scale correlation, and the longitudinal–transverse correlation of the wavelet transforms. At large scales, the flatness factor takes the Gaussian value of 3, and the correlation coefficients vanish. As the scale is decreased from the integral length, the flatness factor and the correlation coefficients start to increase. The increase becomes significant around the Taylor microscale. While the large-scale fluid motions are space-filling and random, the small-scale fluid motions become increasingly sparse and coherent. The small-scale energies are increasingly dominated by those coherent structures. We have also observed that the flatness factor and the scale–scale correlation at small scales are greater in the transverse component than in the longitudinal component.

Wavelet transforms of velocities are large in regions of strong vorticity or strong dissipation. On the other hand, it is known that vorticity and dissipation of turbulence are strong in tube-like regions. With a direct numerical simulation, we have demonstrated that wavelet transforms of velocities are enhanced at the positions of the tubes. The enhancement becomes significant as the scale is decreased. The presence of those structures accounts for the observed enhancements of the flatness factor, the scale–scale, and the longitudinal–transverse correlations. Thus our wavelet analyses have captured the effects of vortex tubes on velocities measured in the experiment, which would be difficult for traditional analysis techniques.

We have done the analyses with five different families of orthonormal wavelets. The results are generally robust with respect to the choice of wavelet. However, there are exceptions. The scale–scale correlation cannot be studied with Haar's and Daubechies' bases. Furthermore, the flatness factor and the longitudinal–transverse correlation of Haar's transforms are equal to those of velocity increments. This is not necessarily the case for the other wavelets. Haar's base is poorly localized in scale and thus unsuitable for general applications. Nevertheless, Haar's base is useful in special applications such as a comparison of wavelet transforms of velocities with scaling-function transforms of vorticity or dissipation.

Finally, we comment on possible discrepancies in wavelet statistics between the experiment with $Re_\lambda = 300$ and the simulation with $Re_\lambda = 43.3$. The flatness factor and the correlation coefficients at the Taylor microscale λ are somewhat higher in the experiment than in the simulation (figures 5, 7, 8 and 11). This feature is attributable to the difference in the Reynolds number. Standard statistical measures such as skewness and flatness of the velocity derivatives suggest that intermittent structures change as the Reynolds number is increased (Van Atta & Antonia 1980; Tabeling *et al.* 1996). Hence wavelet analyses at the higher Re_λ values are of great interest.

We are grateful to A. Hori and Y. Kawashima for their assistance in the experiment, M. Yamada for providing the wavelet algorithm, S. Iwakura for the help in the numerical work, M. Yamada, C. Meneveau, G. Strang for sending us their manuscripts, and M. Umeki, S. Takahashi, T. Uesugi, M. Uchida, and T. Kurokawa for information.

Comments of the referees were helpful in improving the manuscript. T. Fujitani was supported by Granted-in-Aid (B) (1) 06555136 from the Japanese Ministry of Education, Science, and Culture.

Appendix A. Implementation of Harmonic wavelets

Our formulation of discrete Harmonic wavelets is somewhat different from that in the original paper (Mouri & Kubotani 1995). Here we outline the present algorithm. Consider a real input sequence $u[n]$ ($n = 0$ to $2^N - 1$). We first multiply $u[n]$ by $\exp(-\mathrm{i}\pi n/2^N)$:

$$u'[n] = \exp\left(-\frac{\mathrm{i}\pi n}{2^N}\right) u[n] \quad \text{for } n = 0 \text{ to } 2^N - 1. \tag{A 1}$$

The discrete Fourier transformation is applied to the sequence $u'[n]$:

$$u''[m] = 2^{-N/2} \sum_{n=0}^{2^N-1} \exp\left(-\frac{\mathrm{i}2\pi mn}{2^N}\right) u'[n] \quad \text{for } m = 0 \text{ to } 2^N - 1. \tag{A 2}$$

The wavelet transform $\hat{u}_{j,k}$ ($j = 1$ to $N - 1$, $k = 0$ to $2^j - 1$) is calculated from the $u''[m]$ elements with $m = 2^{j-1}$ to $2^j - 1$ and those with $m = 2^N - 2^j$ to $2^N - 2^{j-1} - 1$. These two sequences are combined into a single sequence $u'''[h]$:

$$u'''[h] = \begin{cases} \exp(-\mathrm{i}\varphi)\, u''[h + 2^{j-1}] & \text{for } h = 0 \text{ to } 2^{j-1} - 1 \\ \exp(\mathrm{i}\varphi)\, u''[h - 2^{j-1} + 2^N - 2^j] & \text{for } h = 2^{j-1} \text{ to } 2^j - 1. \end{cases} \tag{A 3}$$

We apply the inverse discrete Fourier transformation to the sequence $u'''[h]$. The results are multiplied by $(-1)^k \exp(\mathrm{i}\pi k/2^j)$. This operation gives

$$\hat{u}_{j,k} = (-1)^k \exp\left(\frac{\mathrm{i}\pi k}{2^j}\right) 2^{-j/2} \sum_{h=0}^{2^j-1} \exp\left(\frac{\mathrm{i}2\pi hk}{2^j}\right) u'''[h]. \tag{A 4}$$

The scaling-function transform $\bar{u}_{J,k}$ ($J = 1$ to $N-1$, $k = 0$ to $2^J - 1$) is tabulated from the $u''[m]$ elements with $m = 0$ to $2^{J-1} - 1$ and those with $m = 2^N - 2^{J-1}$ to $2^N - 1$. These two sequences are again combined into a single sequence $u''''[h]$:

$$u''''[h] = \begin{cases} u''[h] & \text{for } h = 0 \text{ to } 2^{J-1} - 1 \\ u''[h + 2^N - 2^J] & \text{for } h = 2^{J-1} \text{ to } 2^J - 1. \end{cases} \tag{A 5}$$

We apply the inverse discrete Fourier transformation to the sequence $u''''[h]$. The results are multiplied by $\exp(\mathrm{i}\pi k/2^J)$:

$$\bar{u}_{J,k} = \exp\left(\frac{\mathrm{i}\pi k}{2^J}\right) 2^{-J/2} \sum_{h=0}^{2^J-1} \exp\left(\frac{\mathrm{i}2\pi hk}{2^J}\right) u''''[h]. \tag{A 6}$$

Then any signal $u[n]$ can be reconstructed as in (8). The inverse procedures yield the shapes of wavelets and scaling functions from unit vectors in the wavelet representation:

$$w_{j,k}[n] = 2^{1-N/2-j/2} \sum_{m=2^{j-1}}^{2^j-1} \cos\left(2\pi\left(m + \tfrac{1}{2}\right)\left(\frac{n}{2^N} - \frac{k}{2^j}\right) + \varphi\right), \tag{A 7}$$

$$s_{J,k}[n] = 2^{1-N/2-J/2} \sum_{m=0}^{2^{J-1}-1} \cos\left(2\pi\left(m+\tfrac{1}{2}\right)\left(\frac{n}{2^N}-\frac{k}{2^J}\right)\right). \tag{A 8}$$

The wavelet and scaling functions are not periodic with a period of 2^N ($w_{j,k}[2^N] = -w_{j,k}[0]$ and $s_{J,k}[2^N] = -s_{J,k}[0]$). This is due to the operation (A 1). We also note that those functions are not compact in the usual wavenumber domain. The spectra in figure 1(*d*) are from the scalar products with $\exp(\mathrm{i}2\pi(m+\frac{1}{2})n/2^N)$, instead of $\exp(\mathrm{i}2\pi mn/2^N)$.

Harmonic wavelets with different values of φ constitute the same multi-resolution analysis. Transforms at a certain scale for a given value of φ are reproduced from those at the same scale for another value of φ via a unitary transformation. The new transforms follow the same statistical distribution as the original ones, if and only if it is a Gaussian, however (see Lancaster 1954).

Appendix B. Wavelets and band-pass filters

Our discussion is based on the analogy between wavelet transforms and velocity increments, which stems from the nature of wavelets in the space regime (§ 2.3). On the other hand, the nature of wavelets in the wavenumber regime is such that wavelets act as band-pass filters.

The wavelet transformation is defined as the convolution of a signal with some weighting functions. This is equivalent to a multiplication of the Fourier transform of the signal with the corresponding frequency-response functions. The spectral energy distributions of our wavelets are illustrated in figure 1. They all have a band-pass character. Thus wavelet functions split the signal into their spectral components. The scales of the wavelets correspond to the centre frequencies of the band-pass filters, where the higher frequency represents the smaller scale.

To achieve a clear spectral separation, band-pass filters are required to have sharp edges. This is not the case for Haar's base (figure 1*a*). Using Haar's base as a filter leads to a leakage of information among the spectral components. That is why Haar's base gives spurious results for the scale–scale correlation, which reflects the degree of dependence between the individual spectral components (Appendix C). The poor results for the flatness factor and the longitudinal–transverse correlation are explained in the same manner (§ 4).

The band-pass character is merely one aspect of the nature of wavelets. The wavelet transforms are analogous to velocity increments, and are independent of each other. The latter advantage cannot be achieved by digital band-pass filters (Yamada, Kida & Ohkitani 1993). Since the filtering process reduces the number of degrees of freedom, the numerical values of a filtered signal are no longer independent. Hence, compared with usual band-pass filtering techniques, the wavelet transformation offers a straightforward approach to study the space–scale structure of turbulence, especially in statistical analyses.

Appendix C. Wavelet analyses of a random-phase signal

To ensure that our wavelet analyses extract the real properties of turbulence, we examine the transforms of a random-phase signal. The signal has been created by the inverse transformation of the Fourier transforms of the numerical turbulence (§ 5.1), after randomizing their phases uniformly over $[0, 2\pi]$ without changing their

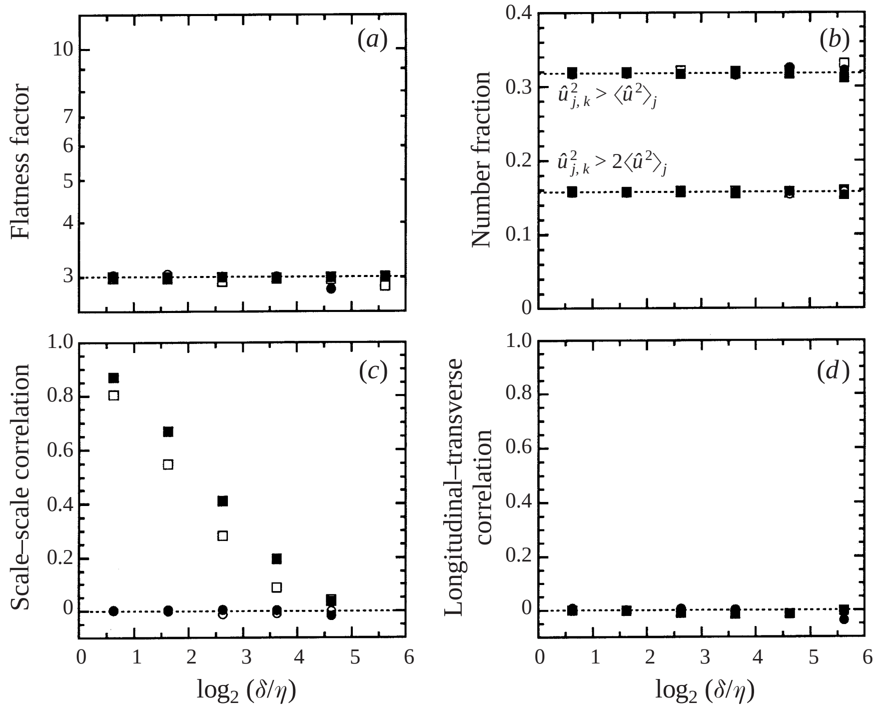

FIGURE 13. Wavelet analyses of a random-phase signal ($M = 3 \times 128^2$, $N = 7$): (*a*) flatness factor defined in (18), (*b*) number fractions of wavelet transforms with $\hat{u}^2_{j,k} > \langle \hat{u}^2 \rangle_j$ and $\hat{u}^2_{j,k} > 2\langle \hat{u}^2 \rangle_j$, (*c*) scale–scale correlation defined in (20), and (*d*) longitudinal–transverse correlation defined in (22). The bases used are Haar's (squares) and Meyer's (circles). The abscissa is the wavelet scale δ. This scale is defined in (13) and normalized by the Kolmogorov length η of the numerical turbulence, from which the random-phase signal has been created. Filled and open symbols in (*a–c*) are for the longitudinal and transverse components. Dotted lines indicate the values expected for a Gaussian random field.

amplitudes and divergence-free property (Yamada & Ohkitani 1991; Kevlahan & Vassilicos 1994). A part of this work has been presented in § 5.1.

Figure 13 illustrates the flatness factor, the number fractions of transforms with $\hat{u}^2_{j,k} > \langle \hat{u}^2 \rangle_j$ and $\hat{u}^2_{j,k} > 2\langle \hat{u}^2 \rangle_j$, the scale–scale correlation, and the longitudinal–transverse correlation ($M = 3 \times 128^2$, $N = 7$). The bases used are Haar's (squares) and Meyer's (circles). The abscissa is the wavelet scale δ, which is defined in (13) and normalized by the Kolmogorov length η of the numerical turbulence. The dotted lines indicate the values expected for a Gaussian random field.

In figure 13(*a*), the flatness factor is equal to the Gaussian value of 3. In figure 13(*b*), the number fractions of transforms with $\hat{u}^2_{j,k} > \langle \hat{u}^2 \rangle_j$ and $\hat{u}^2_{j,k} > 2\langle \hat{u}^2 \rangle_j$ are equal to the Gaussian values. These results are in accord with the central-limit theorem (Sanada 1990; Yamada & Ohkitani 1991). In figure 13(*c*), the scale–scale correlation is absent for Meyer's base. However, for Haar's base, the correlation exists. There is a significant overlap of Haar's functions at adjacent scales in the wavenumber domain (figure 1*a*). The smaller wavenumber in our random-phase signal holds more energy than the larger one, and causes the observed scale–scale correlation. We have actually found that Haar's base yields no scale–scale correlation for a white noise. Finally, in figure 13(*d*), the longitudinal–transverse correlation is absent.

The applications of Daubechies' and Harmonic wavelets to the random-phase signal give the same results as in the case of Meyer's wavelet. Here the end effect has been removed in the Harmonic transformation. The effect is intrinsically absent in Daubechies' and Meyer's transformations, where the basis functions embody the same periodic boundary condition as the random-phase signal.

REFERENCES

Anselmet, F., Gagne, Y., Hopfinger, E. J. & Antonia, R. A. 1984 High-order velocity structure functions in turbulent shear flows. *J. Fluid Mech.* **140**, 63–89.

Argoul, F., Arnéodo, A., Grasseau, G., Gagne, Y., Hopfinger, E. J. & Frisch, U. 1989 Wavelet analysis of turbulence reveals the multifractal nature of the Richardson cascade. *Nature* **338**, 51–53.

Batchelor, G. K. & Townsend, A. A. 1949 The nature of turbulent motion at large wave-numbers. *Proc. R. Soc. Lond.* A **199**, 238–255.

Belin, F., Maurer, J., Tabeling, P. & Willaime, H. 1996 Observation of intense filaments in fully developed turbulence. *J. Phys.* II *Paris* **6**, 573–583.

Champagne, F. H. 1978 The fine-scale structure of the turbulent velocity field. *J. Fluid Mech.* **86**, 67–108.

Daubechies, I. 1988 Orthonormal bases of compactly supported wavelets. *Commun. Pure Appl. Maths* **41**, 909–996.

Douady, S., Couder, Y. & Brachet, M. E. 1991 Direct observation of the intermittency of intense vorticity filaments in turbulence. *Phys. Rev. Lett.* **67**, 983–986.

Farge, M. 1992 Wavelet transforms and their applications to turbulence. *Ann. Rev. Fluid Mech.* **24**, 395–457.

Frisch, U. 1995 *Turbulence: the Legacy of A. N. Kolmogorov.* Cambridge University Press.

Haar, A. 1910 Zur Theorie der orthogonalen Funktionensysteme. *Math. Ann.* **69**, 331–371.

Jiménez, J., Wray, A. A., Saffman, P. G. & Rogallo, R. S. 1993 The structure of intense vorticity in isotropic turbulence. *J. Fluid Mech.* **255**, 65–90.

Kevlahan, N. K.-R. & Vassilicos, J. C. 1994 The space and scale dependencies of the self-similar structure of turbulence. *Proc. R. Soc. Lond.* A **447**, 341–363.

Kolmogorov, A. N. 1941*a* The local structure of turbulence in incompressible viscous fluid for very large Reynolds numbers. *Dokl. Akad. Nauk SSSR* **30**, 301–305.

Kolmogorov, A. N. 1941*b* Dissipation of energy in the locally isotropic turbulence. *Dokl. Akad. Nauk SSSR* **32**, 16–18.

Kolmogorov, A. N. 1962 A refinement of previous hypotheses concerning the local structure of turbulence in a viscous incompressible fluid at high Reynolds number. *J. Fluid Mech.* **13**, 82–85.

Kuo, A. Y.-S. & Corrsin, S. 1971 Experiments on internal intermittency and fine-structure distribution functions in fully turbulent fluid. *J. Fluid Mech.* **50**, 285–319.

Lancaster, H. O. 1954 Traces and cumulants of quadratic forms in normal variables. *J. R. Statist. Soc.* B **16**, 247–254.

Mallat, S. 1989 Multiresolution approximations and wavelet orthonormal bases of $L^2(R)$. *Trans. Am. Math. Soc.* **315**, 69–87.

Meneveau, C. 1991 Analysis of turbulence in the orthonormal wavelet representation. *J. Fluid Mech.* **232**, 469–520.

Meyer, Y. 1985–1986 Principe d'incertitude, bases Hilbertiennes et algèbres d'opérateurs. *Séminaire Bourbaki*, vol. 662.

Moffatt, H. K., Kida, S. & Ohkitani, K. 1994 Stretched vortices – the sinews of turbulence; large-Reynolds-number asymptotics. *J. Fluid Mech.* **259**, 241–264.

Mouri, H. & Kubotani, H. 1995 Real-valued harmonic wavelets. *Phys. Lett.* A **201**, 53–60.

Nelkin, M. 1994 Universality and scaling in fully developed turbulence. *Adv. Phys.* **43**, 143–181.

Newland, D. E. 1993 Harmonic wavelet analysis. *Proc. R. Soc. Lond.* A **443**, 203–225.

Press, W. H., Teukolsky, S. A., Vetterling, W. T. & Flannery, B. P. 1992 *Numerical Recipes in FORTRAN*, 2nd edn. Cambridge University Press.

Sanada, T. 1990 Phase coherency of intermittent turbulence field. *Prog. Theor. Phys.* **84**, 12–17.

SREENIVASAN, K. R. & ANTONIA, R. A. 1997 The phenomenology of small-scale turbulence. *Ann. Rev. Fluid Mech.* **29**, 435–472.

STRANG, G. 1989 Wavelets and dilation equations: a brief introduction. *SIAM Rev.* **31**, 614–627.

TABELING, P., ZOCCHI, G., BELIN, F., MAURER, J. & WILLAIME, H. 1996 Probability density functions, skewness, and flatness in large Reynolds number turbulence. *Phys. Rev.* E **53**, 1613–1621.

TAYLOR, G. I. 1918 On the dissipation of eddies. *R & M Advisory Committee for Aeronautics* **598**.

TAYLOR, G. I. 1938 The spectrum of turbulence. *Proc. R. Soc. Lond.* A **164**, 476–490.

VAN ATTA, C. W. & ANTONIA, R. A. 1980 Reynolds number dependence of skewness and flatness factors of turbulent velocity derivatives. *Phys. Fluids* **23**, 252–257.

YAMADA, M., KIDA, S. & OHKITANI, K. 1993 Wavelet analysis of PDFs in turbulence. In *Unstable and Turbulent Motion of Fluid* (ed. S. Kida), pp. 188–199. World Scientific.

YAMADA, M. & OHKITANI, K. 1991 An identification of energy cascade in turbulence by orthonormal wavelet analysis. *Prog. Theor. Phys.* **86**, 799–815.